Progress In Electromagnetics Research B, Vol. 12, 219–241, 2009

ANALYSIS OF ULTRA-SHORT PULSE PROPAGATION IN NONLINEAR OPTICAL FIBER

M. B. El_Mashade and M. Nady

Electrical Engineering Department, Faculty of Engineering
Al Azhar University
Nasr City, Cairo, Egypt

Abstract—Ultra-short pulse is a promising technology for achieving ultra-high data rate transmission which is required to follow the increased demand of data transport over an optical communication system. Therefore, the propagation of such type of pulses and the effects that it may suffer during its transmission through an optical waveguide have received a great deal of attention in the recent years. Our goal in this paper is to study the propagation characteristics of that pulse in a nonlinear optical fiber. In analyzing these characteristics, the nonlinear effects along with the dispersion are taking into account. Additionally, the considered nonlinear effects include self phase modulation (SPM) and stimulated Raman scattering (SRS). The problem to be processed is modeled using the finite difference time domain (FDTD) technique which represents an efficient tool in achieving the required purpose. Because of the symmetrical structure of the optical waveguide, the FDTD modeling of bodies of revolution (BOR) in cylindrical coordinates is the most preferable algorithm in analyzing our problem. The FDTD treatment of dispersion and nonlinearity of the optical waveguide is accomplished through the direct integration method. In addition, the Lorentzian model is chosen to represent the dielectric properties of the optical fiber. The azimuthal symmetry of optical fiber enables us to use a two-dimensional difference lattice through the projection of the three-dimensional coordinates (r, φ, z) into the (r, z) plane. Extensive numerical results have been obtained for various cavity structures.

Corresponding author: M. B. El_Mashade (ElMashade@Yahoo.Com).

1. INTRODUCTION

Future telecommunication networks would require optical communication systems that can provide error-free transmission at a data rate exceeding Tera-bits per second with a large span that may extend to large distances over an optical waveguide without electronic signal regeneration. The main challenges for achieving such high data rate systems lie in pulse generation, dispersion and loss compensation, and nonlinearity management. Reduction of the pulse width increases the information rate that can be transmitted and this consequently leads to significant increase in our ability to perform high-speed digital communications and offers the potential for faster computational devices. Thanks to the quantum structure of some semiconductor materials, quantum cascade (QC) lasers can generate ultra-short pulses by gain switching and active and passive mode-locking of this type of semiconductor lasers due to the short relaxation times of electrons and the photon lifetime; both are of the order of a picosecond in these lasers. On the other hand, due to the huge bandwidth and the high instantaneous power associated with ultra-short pulses, dispersion and nonlinearity represent critical issues for their practical applications [1–10].

Although the new manufacturing techniques of fabrication of optical fiber have minimized its loss, long haul transmission still requires high power optical amplifiers to compensate for the fiber loss. In this situation, the pulse distortion due to the fiber nonlinearity should be considered. On the other hand, dispersion is the spreading, in the time domain, of a signal pulse as it travels through an optical waveguide. From the spectral point of view, this means that the spectral components of the propagating pulse reach their destination at slightly different times. Both fiber's loss and dispersion affect the repeater spacing and the bandwidth of a long distance optical communication system. Therefore, maintaining low dispersion is of equal importance for ensuring increased system information capacity.

As the pulse width becomes shorter, our ability to accurately model the propagation of the pulse becomes more complicated. Therefore, it was necessary to develop a computational electromagnetic tool that is capable of accurately modeling the propagation of pulses with widths of the order of several femtoseconds. The propagation of pulses of shorter widths has some significant consequences. Firstly, as the width of the pulse becomes shorter, its bandwidth becomes larger and the dispersion property of the materials used to propagate it becomes effective. Secondly, the propagation of these ultra-short pulses needs to include the nonlinear effects of the media in which they propagate. In other words, as the pulse becomes shorter, the nonlinear

nature of the waveguide materials has a more significant contribution on its propagation.

The nonlinear behavior of electromagnetic fields in optical fiber is due to the nonlinear relation between the electric field and the induced electric polarization. Different approximations have been suggested to yield an analytical solution for Maxwell's equations for the case of electromagnetic problems. The most popular one of these approximations is to formulate the problem as a set of scalar nonlinear equations with slowly varying envelope. These non-linear equations have the form of non-linear Schrödinger's equation (NLSE) which can be solved either analytically or numerically. The analytical version of these solutions, for very little special cases, is obtained by using the method of inverse scattering transformation [5]. The numerical solution, on the other hand, is carried out by different methods such as split step Fourier method and the beam propagation method [1]. However, these approximations are based mainly on the assumption that the temporal variation of the envelope is relatively small with respect to the carrier and this condition is not fulfilled in the case of ultra-short pulse. Due to the rapid increase in computational capabilities, finite-difference time-domain (FDTD) technique has become a fertilized alternative method to study such type of complex problems.

Based on the previous discussion, it is necessary to develop a full-wave analysis for Maxwell's vector field equations taking into account the effects of dispersion and nonlinearity. Solving 1-D nonlinear Maxwell's equations by using FDTD was discussed by several authors [3–7]. In their solutions, they used different techniques to include the nonlinear effect in the FDTD formulation such as z-transform [4], recursive convolution method [5], and direct integration method [6, 7]. Although the 3-D formulation of that problem represents a more practical view of applications, the direct solution using 3D-FDTD requires huge storage and computational time. Different techniques have been introduced [8, 9] to simplify this case of the problem under investigation to become more suitable for simulation by using the available computational resources. Scalar FDTD, moving frame technique, and parallel processing are the most familiar candidates of these techniques.

Another significant simplified treatment of this problem can be obtained by using the rotational symmetry of the optical fiber's geometry. In this treatment, the azimuthal dependence of the field components would be represented by a Fourier series expansion and it would be sufficient to simulate the problem at a single ϕ-plane in cylindrical coordinates. This technique is known as FDTD of

bodies of revolution BOR-FDTD [15]. It was already used to solve the problem in a type of optical fiber which is free of dispersion and non-linearity [12]. Additionally, it was employed to solve bodies of revolution of dispersive material [14]. The scope of our manuscript is to introduce an extension of this BOR-FDTD technique to combine the nonlinear effects with the dispersion effect and to show their influence on the behavior of an ultra-short pulse as it propagates over an optical fiber. This paper is organized as follows: Section 2 formulates the problem under consideration after presenting the basic assumptions which are taking into account in this formulation. The outlines of the proposed algorithm for solving this problem are explained in Section 3. Section 4 is devoted to the presentation of our numerical simulation results and Section 5 summarizes our concluded remarks.

2. BASIC ASSUMPTIONS AND PROBLEM FORMULATION

In this section, we are concerned with formulating our problem and stating the basic assumptions under which this formulation was achieved. The backbone of any electromagnetic problem is the coupled Maxwell's relations. They describe the variation of the electric field of this problem as a function of its associated magnetic field. Let us now start our analysis by writing these two coupled equations:

$$\nabla \times \vec{E} = -\mu \frac{\partial \vec{H}}{\partial t} \tag{1a}$$

and

$$\nabla \times \vec{H} = \frac{\partial \vec{D}}{\partial t} + \sigma \vec{E} \tag{1b}$$

In the above expressions, $\vec{E}$ and $\vec{H}$ represent the electric and magnetic field vectors, respectively; μ and σ denote the permeability and conductivity of the medium in which the pulse propagates. In the case where this medium is of type nonlinear, the electric field displacement $\vec{D}$ is related to the electric field through the formula [12]:

$$\vec{D} = \varepsilon_0 \varepsilon_\infty \vec{E} + \vec{P}_{LN} + \vec{P}_{NL} \tag{2}$$

ε_0 and ε_∞ represent the free space and the medium relative permittivity at infinite frequency, respectively. The linear $\vec{P}_{LN}$ and

nonlinear $\vec{P}_{NL}$ polarization vectors are defined as [9]:

$$\vec{P}_{\xi LN}(r,t) = \varepsilon_0 \int_{-\infty}^{\infty} \chi^{(1)}\left(t-t'\right)\, \vec{E}_{\xi}\left(r,t'\right) dt' \tag{3a}$$

and

$$\begin{aligned} \vec{P}_{\xi NL}(r,t) \;=\; & \varepsilon_0 \iiint_{-\infty}^{\infty} \chi^{(3)}\left(t-t_1, t-t_2, t-t_3\right) \\ & \vec{E}_{\xi}(r,t_1)\, \vec{E}_{\xi}(r,t_2)\, \vec{E}_{\xi}(r,t_3)\, dt_1\, dt_2\, dt_3 \end{aligned} \tag{3b}$$

where ξ represents either r-, φ- or z-component in cylindrical coordinates; $\chi^{(1)}(t)$ and $\chi^{(3)}(t)$ denote the 1st- and the 3rd-order susceptibility functions, respectively, which are assumed to be independent of the direction of the electric field. It is well known that the 2nd-order, $\chi^{(2)}(t)$, along with all even orders of susceptibility functions, equals to zero in media that display inversion symmetry in its crystal structure. It is of importance to note that the optical fiber is fabricated from one of these materials [14].

The key point of the BOR_FDTD is the analytical introduction of the azimuthally field variation. Assuming that the non-linear response of the material is also rotationally symmetric, the field components can

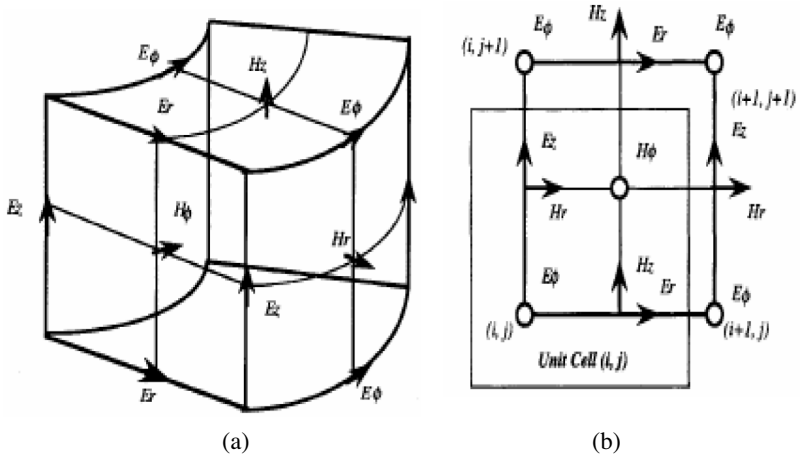

(a) (b)

Figure 1. Field component locations in finite difference representation. (a) 3-D representation in cylindrical coordinates. (b) Corresponding 2.5-D problem by factoring out the ϕ dependence.

be expanded in a Fourier series as:

$$\vec{\xi}(r,\varphi,z,t) = \sum_{m=0}^{\infty} \left[\vec{\xi}_{me}(r,z,t)\cos(m\varphi) + \vec{\xi}_{mo}(r,z,t)\sin(m\varphi) \right] \quad (4)$$

In the above expression, $\vec{\xi}$ stands for either $\vec{H}$ or $\vec{D}$ field vector. The suffix m represents the mode number along the φ direction and the suffix e or o represents either even or odd mode.

Substituting the displacement and magnetic field vectors, which have special cases of Eq. (4), into Eq. (1), a new set of equations will be obtained after factoring out the angular variable φ. These new equations are referred to as 2.5-D versions of the original formula (Eq. (1)). 2.5-D means six field components in 2-dimensional plane; i.e., the six field components will be computed in a specified direction of φ-plane. The locations of the electric and magnetic fields in the original 3-D and in 2.5-D situations are shown in Fig. 1. Then, following the same notations as those used in the conventional FDTD [15], the finite-difference form of this new set of equations can be formulated as:

$$D_r^{n+1}(i,j) = D_r^n(i,j) - \left(\frac{\Delta t}{\Delta z}\right)\left(H_\varphi^{n+1/2}(i,j) - H_\varphi^{n+1/2}(i,j-1)\right) - \left(\frac{m*\Delta t}{i*dr}\right) H_z^{n+1/2}(i,j) \quad (5a)$$

$$D_\varphi^{n+1}(i,j) = D_\varphi^{n+1}(i,j) + \left(\frac{\Delta t}{\Delta z}\right)\left(H_r^{n+1/2}(i,j) - H_r^{n+1/2}(i,j-1)\right) - \left(\frac{\Delta t}{\Delta r}\right)\left(H_z^{n+1/2}(i,j) - H_z^{n+1/2}(i-1,j)\right) \quad (5b)$$

$$D_z^{n+1}(i,j) = D_z^{n+1}(i,j) + \left(\frac{m*\Delta t}{(i-1/2)\Delta r}\right) H_r^{n+1/2}(i,j) + \left(\frac{\Delta t}{(i-1/2)\Delta r}\right)\left(i*H_\varphi^{n+1/2}(i,j) - (i-1)*H_\varphi^{n+1/2}(i-1,j)\right) \quad (5c)$$

$$H_r^{n+1/2}(i,j) = H_r^{n+1/2}(i,j) - \left(\frac{m*\Delta t}{\mu_0 (i-1/2)\Delta r}\right) E_z^n(i,j) + \left(\frac{\Delta t}{\mu_0 \Delta z}\right)\left(E_\varphi^n(i,j+1) - E_\varphi^n(i,j)\right) \quad (5d)$$

$$H_\varphi^{n+1/2}(i,j) = H_\varphi^{n+1/2}(i,j) - \left(\frac{\Delta t}{\mu_0 \Delta z}\right)\left(E_r^n(i,j+1) - E_r^n(i,j)\right) + \left(\frac{\Delta t}{\mu_0 \Delta r}\right)\left(E_z^n(i+1,j) - E_z^n(i,j)\right) \quad (5e)$$

$$H_z^{n+1/2}(i,j)=H_z^{n+1/2}(i,j)+\left(\frac{m*\Delta t}{\mu_0*i*\Delta r}\right)E_r^n(i,j)$$
$$-\left(\frac{\Delta t}{\mu_0*i*\Delta r}\right)\left((i+1/2)E_\varphi^n(i+1,j)-(i-1/2)E_\varphi^n(i,j)\right) \quad (5f)$$

where

$$r=\Delta r\left(i-\frac{1}{2}\right), \quad z=j*\Delta z, \quad \text{and } t=n*\Delta t \quad (5g)$$

The next step in this analysis is to search how the singularity in Eq. (5), as $r \to 0$, can be handled. This problem of singularity was solved by Chen et al. [15]. It was assumed that only one-half of the first cell $(0, j)$ is located in the computational domain as shown in Fig. 2. This figure demonstrates that all the three components, E_r, H_z, and H_φ exist for $i = 0$. However, as seen from Eqs. (5b) and (5c), only the tangential components to this boundary, i.e., H_z, and H_φ are needed to update the adjacent D_φ and D_z fields internal to this mesh, i.e., cell $(1, j)$. Furthermore, from Eq. (5c), it is shown that to compute D_z at $i = 1$, H_φ at $i = 0$ must be multiplied by a factor $(i - 1)$ which is zero. Hence, H_φ at $i = 0$ is not needed. Thus, only H_z is needed at the boundary $i = 0$ to update all field components in the computational domain. It is of importance to note that, from Eq. (5b), H_z vanishes at $i = 0$ for $m \neq 0$. Consequently, the only one needed to be evaluated is H_z for $i = 0$ and $m = 0$. The starting point to this evaluation is the

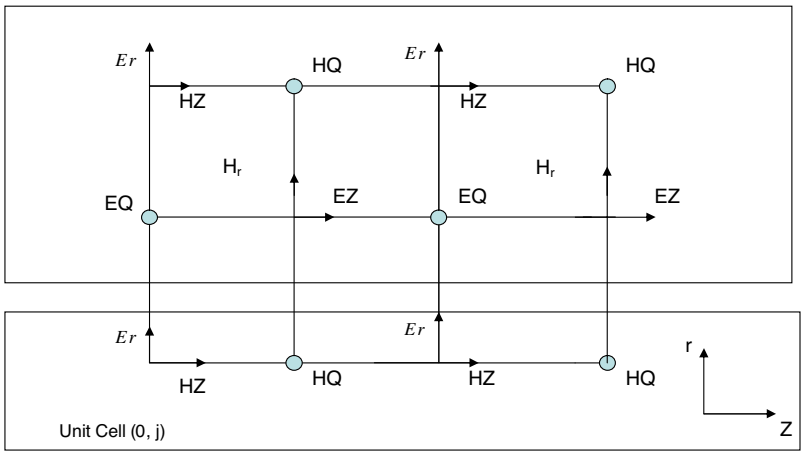

Figure 2. A section of the FDTD lattice at $r = 0$.

integral form of Faraday's law which is:

$$\oint_{\Delta c} \vec{E} \cdot d\vec{l} = -\iint_{\Delta s} \mu \frac{\partial \vec{H}}{\partial t} \cdot d\vec{s} \tag{6}$$

The contour of integration Δc is taken as a loop around the z-axis with radius $r_0 = \Delta r/2$ and Δs denotes an element area inside the loop, as shown in Fig. 3. Now, apply Eq. (6) to the magnetic field H_z at the z-axis and the electric field E_φ around it. It is important to note that the electric field E_φ varies sinusoidally with φ, as previously mentioned. For $m = 0$, the electric field $E_\varphi^n(0, j)$ is assumed to be constant over the integral path, so Eq. (6) becomes:

$$2\pi \frac{dr}{2} E_\varphi^n = -\mu\pi \left(\frac{dr}{2}\right)^2 \frac{H_z^{n+1/2} - H_z^{n-1/2}}{dt} \tag{7}$$

After simplifying this equation, the following time update formula for H_z at $i = 0$ and $m = 0$ is obtained

$$H_z^{n+1/2}(0, j) = H_z^{n-1/2}(0, j) - \frac{4dt}{\mu dr} E_\varphi^n(1, j) \tag{8}$$

Once H_z is computed at $i = 0$, the rest of the field components can be easily evaluated, as Eq. (5) demonstrates.

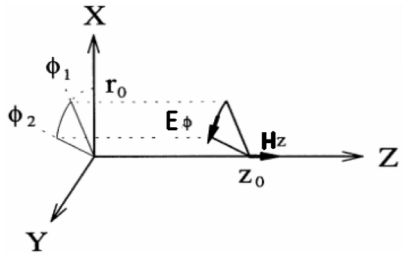

Figure 3. Integral path for the evaluation of H_z at $r = 0$.

3. FDTD ALGORITHM FOR NONLINEAR DISPERSIVE MATERIALS

In the previous section, we have formulated the finite difference basic equations that govern the variation of the new magnetic field as a function of the old electric and magnetic field components, Eqs. (5d) and (5f), and that control the variation of the new displacement field

with the old displacement and magnetic field components (Eqs. (5a) and (5c)). Our goal in this section is to obtain the new electric field components as a function of the displacement and polarization fields. In nonlinear optics, the relation between the displacement vector $\vec{D}$ and electric field vector $\vec{E}$ depends on the linear and nonlinear polarization characteristics of the underlined medium, as Eq. (2) demonstrates.

To complete our analysis, a particular models for $\chi^{(1)}(t)$ and $\chi^{(3)}(t)$ must be firstly proposed. Here, a Lorentzian model is chosen to represent the linear dispersive susceptibility of the considered material. The frequency-domain representation of such a model has a form given by:

$$\chi^{(1)}(\omega) = \frac{(\varepsilon_s - \varepsilon_\infty)\,\omega_0^2}{\omega_0^2 + 2j\omega\delta - \omega^2} \tag{9}$$

Furthermore, the material nonlinearity is taken as:

$$\vec{P}_{NL}(r,z,t) = \varepsilon_0 \chi^{(3)} \vec{E}(r,z,t) \int_{-\infty}^{\infty} g(t-\bar{t})\, E^2(r,z,\bar{t})\, d\bar{t} \tag{10}$$

In the above formula, $\chi^{(3)}$ represents the nonlinear coefficient. The causal response function $g(t-\bar{t})$ is normalized in such a way that its integration over all the possible time values becomes unity. In other words, this function can be defined as

$$g(t) = \alpha\delta(t) + (1-\alpha)\; g_R(t) \tag{11}$$

In this relation, $\delta(t)$ is the Dirac delta function representing the instantaneous response of Kerr interaction; α is a weighting factor that weights the relation between the Kerr and the Raman interactions; and $g_R(t)$ is defined as:

$$g_R(t) = \left(\frac{\tau_1^2 + \tau_2^2}{\tau_1 \tau_2^2}\right) \exp(-t/\tau_2) \sin(t/\tau_1) \tag{12}$$

It models a single Lorentzian line (single-pole) centered on the optical phonon frequency, $1/\tau_1$, and having a linewidth of $1/\tau_2$. In FDTD method, there are different techniques dealing with Eq. (2) to compute the new electric field. Among them, there are Z-transform technique, recursive convolution method, and auxiliary differential equation method which is known as direct integration method. Due to its high precision, the last technique is chosen here to carry out our analysis. It derives a system of coupled second order differential equations, the

solution of which can be handled by defining two auxiliary functions $F(t)$ and $G(t)$ that are proposed by Goorjian and Taflove [6]. Thus,

$$F_J(t) = \varepsilon_0 \int_0^t \chi_J^{(1)}(t-\bar{t})\, E(r,z,\bar{t})\, d\bar{t} \quad J = 1, 2, \ldots, p \tag{13}$$

p in the above expression denotes the number of poles

$$G(t) = \varepsilon_0 \int_0^t g_R(t-\bar{t})\, E^2(r,z,\bar{t})\, d\bar{t} \tag{14}$$

Using the definitions of $F(t)$ and $G(t)$, Eq. (2) becomes

$$E = \frac{D - \sum_j F_j - (1-\alpha)\chi^{(3)} E\, G}{\varepsilon_0 \left[\varepsilon_\infty + \alpha\chi^{(3)}(E)^2\right]} \tag{15}$$

The functions $F(t)$ and $G(t)$ have the property that satisfies the following coupled second-order differential equations

$$\frac{1}{\omega_0^2}\frac{d^2F}{dt^2} + \frac{2\delta}{\omega_0^2}\frac{dF}{dt} + \left[1 + \frac{\varepsilon_s - \varepsilon_\infty}{\varepsilon_\infty + \alpha\chi^{(3)}(E)^2}\right] F + \left[\frac{(\varepsilon_s - \varepsilon_\infty)(1-\alpha)\chi^{(3)}E}{\varepsilon_\infty + \alpha\chi^{(3)}(E)^2}\right] G = \left[\frac{\varepsilon_s - \varepsilon_\infty}{\varepsilon_\infty + \alpha\chi^{(3)}(E)^2}\right] D \tag{16}$$

$$\frac{1}{\bar{\omega}_0^2}\frac{d^2G}{dt^2} + \frac{2\bar{\delta}}{\omega_0^2}\frac{dG}{dt} + \left[1 + \frac{(1-\alpha)\chi^{(3)}(E)^2}{\varepsilon_\infty + \alpha\chi^{(3)}(E)^2}\right] G + \left[\frac{E}{\varepsilon_\infty + \alpha\chi^{(3)}(E)^2}\right] F = \left[\frac{E}{\varepsilon_\infty + \alpha\chi^{(3)}(E)^2}\right] D \tag{17}$$

The finite difference form of this system of coupled equations, for the r-component, becomes:

$$\frac{1}{\omega_0^2(\Delta t)^2}\left(F_r^{n+1}(i,j) - 2F_r^n(i,j) + F_r^{n-1}(i,j)\right) + \frac{\delta}{\omega_0^2\Delta t}\left(F_r^{n+1}(i,j) - F_r^{n-1}(i,j)\right) + \left[1 + \frac{\varepsilon_s - \varepsilon_\infty}{\varepsilon_\infty + \alpha\chi^{(3)}(E_r^n(i,j))^2}\right]\frac{F_r^{n+1}(i,j) + F_r^{n-1}(i,j)}{2}$$

$$+\left[\frac{(\varepsilon_s-\varepsilon_\infty)(1-\alpha)\chi^{(3)}E_r^n(i,j)}{\varepsilon_\infty+\alpha\chi^{(3)}\left(E_r^n(i,j)\right)^2}\right]\frac{\left(G_r^{n+1}(i,j)+G_r^{n-1}(i,j)\right)}{2}$$
$$=\left[\frac{\varepsilon_s-\varepsilon_\infty}{\varepsilon_\infty+\alpha\chi^{(3)}\left(E_r^n(i,j)\right)^2}\right]\frac{\left(D_r^{n+1}(i,j)+D_r^{n-1}(i,j)\right)}{2} \quad (18)$$

and

$$\frac{1}{\bar{\omega}_0^2(\Delta t)^2}\left(G_r^{n+1}(i,j)-2G_r^n(i,j)+G_r^{n-1}(i,j)\right)$$
$$+\frac{\bar{\delta}}{\bar{\omega}_0^2\Delta t}\left(G_r^{n+1}(i,j)-G_r^{n-1}(i,j)\right)$$

$$+\left[1+\frac{(1-\alpha)\chi^{(3)}\left(E_r^n(i,j)\right)^2}{\varepsilon_\infty+\alpha\chi^{(3)}\left(E_r^n(i,j)\right)^2}\right]\frac{\left(G_r^{n+1}(i,j)+G_r^{n-1}(i,j)\right)}{2}$$
$$+\left[\frac{E_r^n(i,j)}{\varepsilon_\infty+\alpha\chi^{(3)}\left(E_r^n(i,j)\right)^2}\right]\frac{\left(F_r^{n+1}(i,j)+F_r^{n-1}(i,j)\right)}{2}$$
$$=\left[\frac{E_r^n(i,j)}{\varepsilon_\infty+\alpha\chi^{(3)}\left(E_r^n(i,j)\right)^2}\right]\frac{\left(D_r^{n+1}(i,j)+D_r^{n-1}(i,j)\right)}{2} \quad (19)$$

Then, these simultaneous equations are solved for F_r^{n+1} and G_r^{n+1} to give the new value of electric field which can be obtained by applying Newton iteration method to the Eq. (15). Thus,

$$E_r^{k+1}(i,j)=\frac{D_r^{n+1}(i,j)-\sum_J F_{r_J}^{n+1}(i,j)-(1-\alpha)\chi^{(3)}E_r^k(i,j)G_r^{n+1}(i,j)}{\varepsilon_0\left[\varepsilon_\infty+\alpha\chi^{(3)}\left(E_r^k(i,j)\right)^2\right]} \quad (20)$$

The staring value for this iteration would be the calculated field at the previous time step E_ξ^n. After sufficient k iterations, the difference between E_ξ^{k+1} and E_ξ^k would be negligible which corresponds to convergent solution. At this point the electric field E_ξ^{k+1} would correspond to the new electric field component E_ξ^{n+1}. On the other hand, Eq. (20) can be combined with the auxiliary functions $F_\xi(t)$ and $G_\xi(t)$ to represent the modification that is introduced here, on the traditional BOR-FDTD method, to include the nonlinearity and dispersion effects. The term $(1-\alpha)\chi^{(3)}E_\xi^k(i,j)G_\xi^{n+1}(i,j)$ in Eq. (20) corresponds to the stimulated Raman scattering (SRS) effect.

This effect can be canceled by setting α equal unity. The term $\alpha\chi^{(3)}(E_\xi^k(i,j))^2$ in the same equation, on the other hand, corresponds to the self phase modulation (SPM). Setting α equal zero would cancel this SPM, which is practically unaccepted. The above two terms are related to the nonlinear effects in optical fiber and can be canceled by eliminating $\chi^{(3)}$. Finally, the $F_\xi(i,j)$ term represents the dispersion effect.

The proposed algorithm for solving the above complicated system of mathematical equations can be summarized as follows: the updating process starts with the calculation of the new values of the magnetic field components on all the grid points of the computational domain using Eqs. (5d) and (5f). By means of these values, the displacement field components are updated in the same way using Eqs. (5a) and (5c). Subsequently, new values of the electric field components are calculated with reference to Eq. (20). This approach avoids the necessity of updating the dielectric values of the material, which arising due to the nonlinear effects, in the computational domain because these effects are directly taken into account in calculating the electric field components, through the computation of Eq. (20).

The numerical algorithm of the finite differences described above requires a specific relation between time increment dt and spatial increment of the lattice. This relation is necessary to avoid numerical instability, which means increasing the results without limit as time progress. In BOR_FDTD, the numerical stability restriction on the choice of the spatial and time increments is given by:

$$c\Delta t \leq \frac{\min(\Delta r, \Delta z)}{s} \tag{21}$$

where c is the speed of light in the medium, $s = \sqrt{2}$ for $m = 0$, and $s = m + 1$ for $m > 0$. In our numerical calculations, a length of one wavelength is divided into 30 spatial increments (spatial increment = $\lambda/30$) to avoid numerical dispersion.

The present simulation results are based on the ratio of the total field to the scattered field (TF/SF) excitation technique [11]. The source signal of this excitation is assumed to be a sinusoidally modulated pulse with spatial Gaussian distribution of the form:

$$A(r,t) = A_0 \frac{\sin(2\pi ct/\lambda_c)}{\cosh\left(\sqrt{2}(t-4T_e)/T_e\right)} \exp\left(-(r/r_0)^2\right) \tag{22}$$

In Eq. (22), λ_c is the carrier wavelength in free space and T_e is the pulse width. This spatial Gaussian distribution corresponds nearly to the field distribution of the fundamental mode in optical fiber [16]. Our

numerical results are carried out for a pulse width (FWHM) of 20 fs and a carrier wavelength of 2.2 μm. On the other hand, r_0 denotes the radius of the fundamental mode. This radius has a mathematical form given by [9]

$$r_0 = a\left(0.65 + 1.619V^{-1.5} + 2.879V^{-6}\right) \tag{23}$$

where a is the core radius and V is the normalized parameter defined by

$$V = \frac{2\pi a}{\lambda}\sqrt{\varepsilon_{core} - \varepsilon_{cladd}} \tag{24}$$

To truncate the computational domain of the FDTD algorithm, it is required to use an appropriate absorbing boundary condition. The most effective absorbing boundary condition is the perfect matched layer (PML). However, the formulation of PML in the r-direction would be a quite complicated problem for nonlinear material as in the case of our problem. Fortunately, the field is naturally decaying in the cladding region in such a way that it would be quite sufficient to use a simpler absorbing boundary condition for the geometrical specification of the optical fiber. Thus, the results of the present paper are based on Mur's absorbing boundary condition which has much simpler form in comparison with PML.

4. NUMERICAL SIMULATION RESULTS

After the presentation of our analysis for the propagation characteristics of an ultra-short pulse in an optical waveguide of nonlinear behavior, the next logical step is to program the obtained mathematical formulas on a digital computer to follow the movement of that pulse and to show its shape variation as it progresses through the optical fiber. Some numerical values must be given to the program for running. Our numerical results are obtained for a 20 fs FWHM input secant pulse at 2.2 μm carrier wavelength. This pulse propagates in a single pole material; the parameters of which are introduced in Table 1, as a core material and the cladding material has a refractive index which is 1% less than that of the core material. The radius of the core is assumed to be 4.5 μm while the radius of the cladding is taken as 7.5 μm. The displayed results are divided into two categories of curves. The first category contains Figs. 4–8 while the second one consists of Figs. 9–13. In the first group, the linear effects are the only effects that are taken into account. In the second group, on the other hand, both the linear and nonlinear effects are considered in evaluating its candidates of figures.

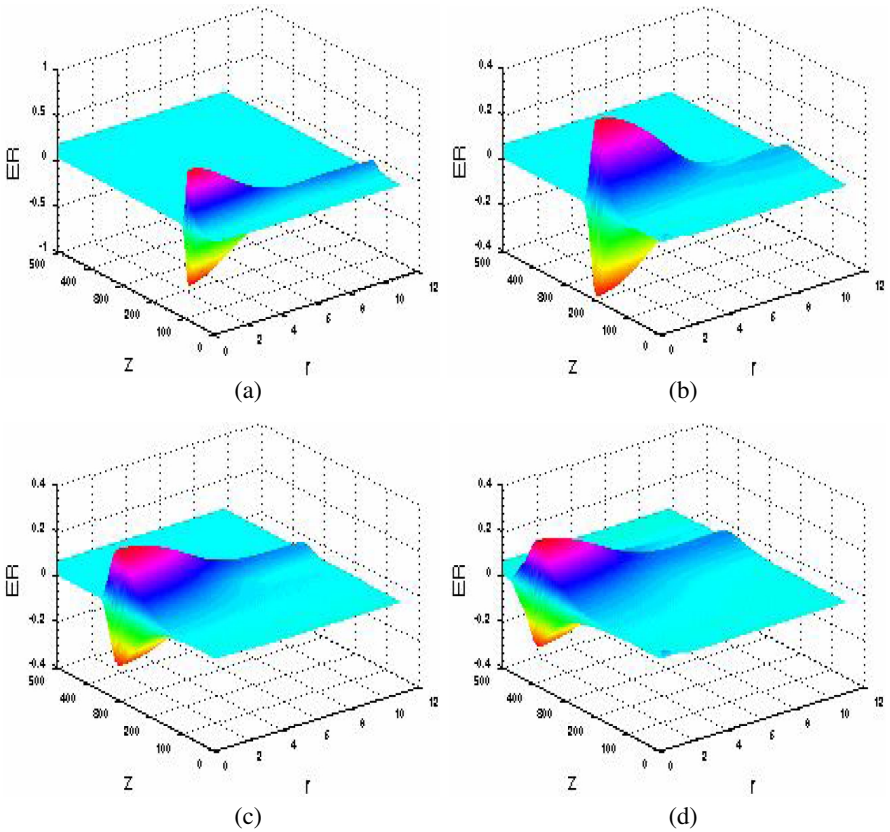

Figure 4. Spatial variation of E_r, for fixed φ angle of 30°, at instants of: (a) 675 fs, (b) 1475 fs, (c) 2125 fs, (d) 3250 fs.

Table 1. Lorentz parameters of single-pole material.

Static permittivity ε_s	5.25
Infinite permittivity ε_∞	2.25
Resonant frequency ω_0	4×10^{14} rad/sec
Damping coefficient δ	2 GHz

Let us start our discussion about the behavior of each one of the figures of the first group. The family of curves of Fig. 4 shows the variation of radial component of the electric field "E_r", as a function of r and z at an azimuthal angle of 30° with time. Figs. 4(a)–

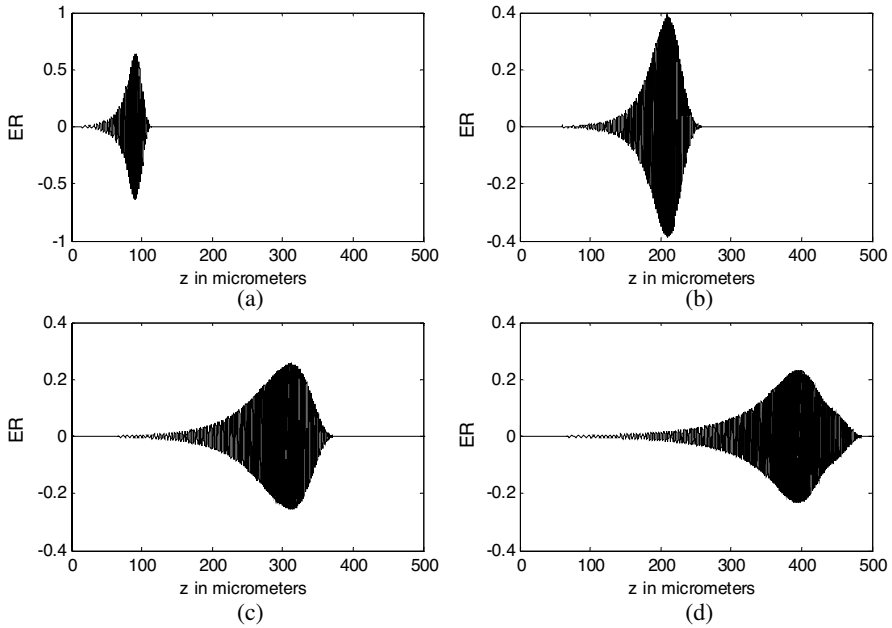

Figure 5. Axial variation of the electric field radial component (E_r) at instants of: (a) 675 fs, (b) 1475 fs, (c) 2125 fs, (d) 3250 fs.

4(d) illustrate these variations at instants of 675, 1475, 2125, and 3250 fsec., respectively. From these figures, it is shown that as the pulse propagates through the optical waveguide, it suffers from dispersion. The characteristics of this dispersion are clearly demonstrated on the shape of the pulse where its amplitude decreases as its distance of propagation increases and its width broadens. It is of importance to note that the scale of the amplitude axis in Fig. 4(a) is different from that of Figs. 4(b)–4(d), where it varies from -1 to $+1$ in the first scene while it changes from -0.4 to $+0.4$ in the other scenes. For these characteristics to be explicitly clear, we repeat the presentation of the same candidates of Fig. 4 as a surface scenes instead of volume scenes by fixing the radial coordinate (r = const.). Figs. 5(a)–5(d) illustrate the variation of E_r with z at the same instant values as in Fig. 4 taking into account that r and φ are held constants. The amplitude axis in each scene of this figure is the same as its corresponding one in the previous figure. The displayed results of this figure demonstrate clearly the effect of dispersion on the behavior of the propagated pulse where its width increases and its amplitude decreases as it travels along the optical waveguide. In the next family of curves,

we are concerned with the intensity variation of the hybrid mode of propagation (HE_{11}) as a function of r at the same instant values as the previous figures. Since the considered optical fiber is of monomode type, the HE_{11} mode represents the fundamental mode of propagation. The obtained results for these operating conditions are shown in Figs. 6(a)–6(d). It is evident from the behavior of the intensity of the mode under consideration that it maintains its peak always at the center of the guide and decays as the radial distance increases. The rate of decreasing is approximately unchanged while the peak amplitude goes lower as the pulse travels along the waveguide, as we have previously mentioned. The next candidate in the category under investigation, which associates with the time-domain representation, deals with the variation of the radial electric field component with time, for different values of z, given that r & φ are maintained unchanged. Figs. 7(a)–7(c) depict this variation at regular intervals of z, which are 75, 150, and 225 μm. This is also another way to demonstrate the concept of dispersion. In the final figure of this category, it is required to spectrally analyze the radial electric field associated with the pulse

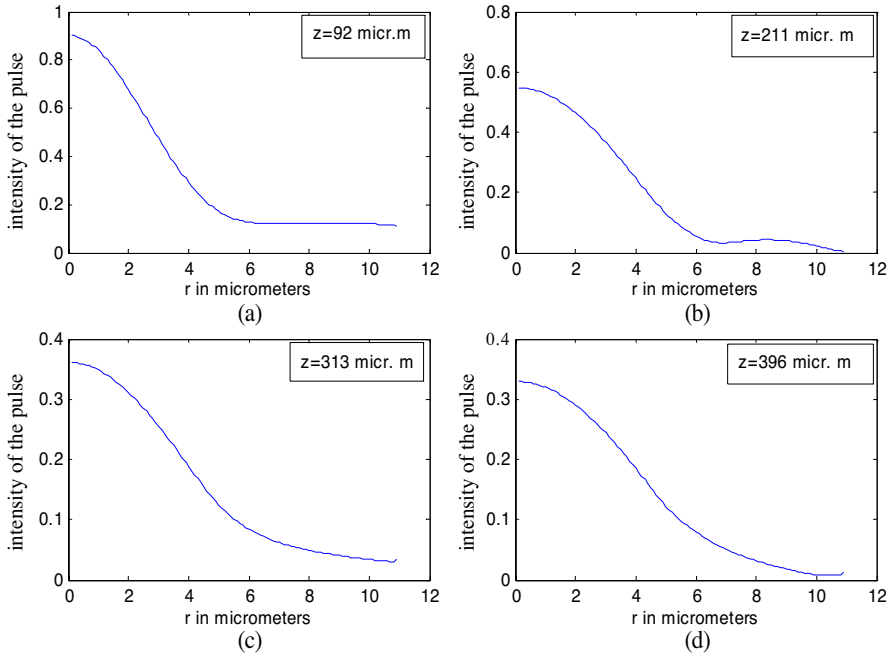

Figure 6. Intensity variation corresponds to the peak of the pulse at instants of: (a) 675 fs, (b) 1475 fs, (c) 2125 fs, (d) 3250 fs.

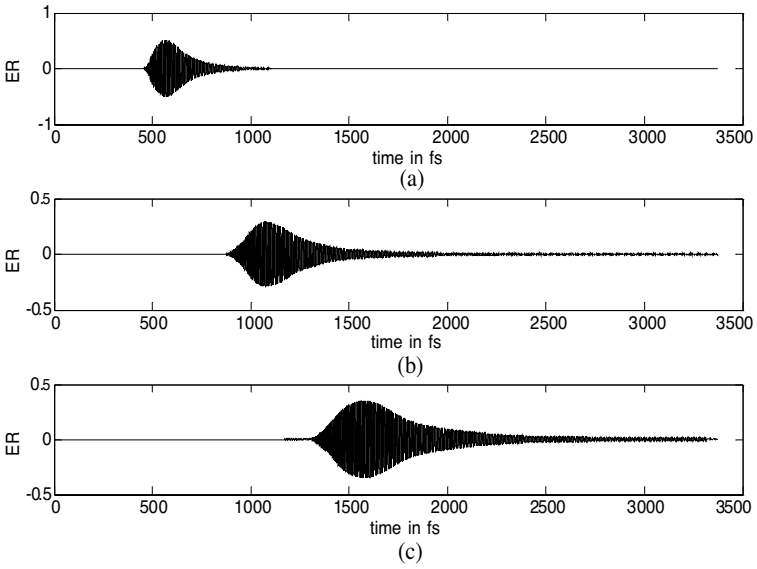

Figure 7. Temporal variation of the electric field radial component (E_r) at different points on the axis and corresponds to: (a) $z = 75\,\mu\text{m}$ (b) $z = 150\,\mu\text{m}$ (c) $z = 225\,\mu\text{m}$.

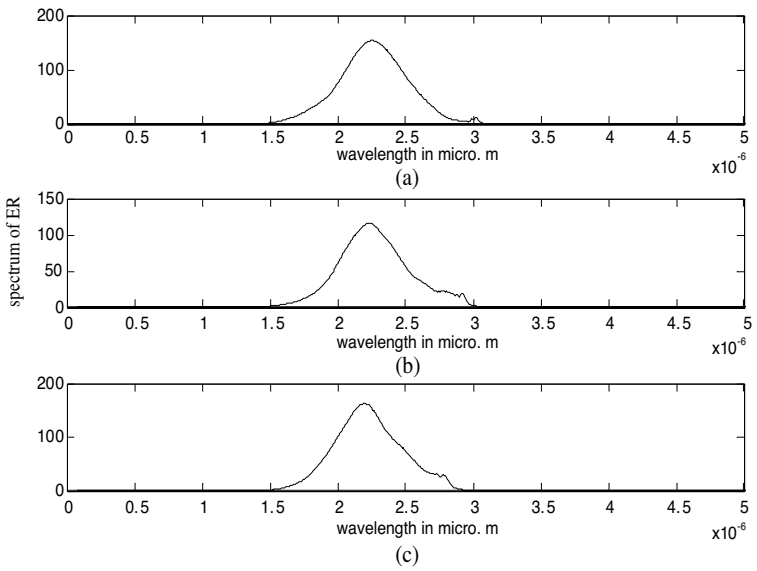

Figure 8. Spectrum of E_r at different points on the axis and at z equals: (a) $75\,\mu\text{m}$ (b) $150\,\mu\text{m}$ (c) $225\,\mu\text{m}$.

to show its frequency contents. The frequency-domain representations of Figs. 7(a)–7(c) are illustrated in Figs. 8(a)–8(c), respectively. The spectrum shown in these figures demonstrates that the frequency content of E_r has a resonance curve with its center located around $\lambda = 2.2\,\mu\text{m}$, which is the central frequency of the input pulse, and approximately maintains its shape through out the z-axis, except a slightly variation of its peak.

In the second category of curves, we repeat the drawing of the same family of curves as in the first category except that the nonlinear effects along with the linear ones are taken into account in evaluating its numerical results. The numerical values of the nonlinear parameters are taken as:

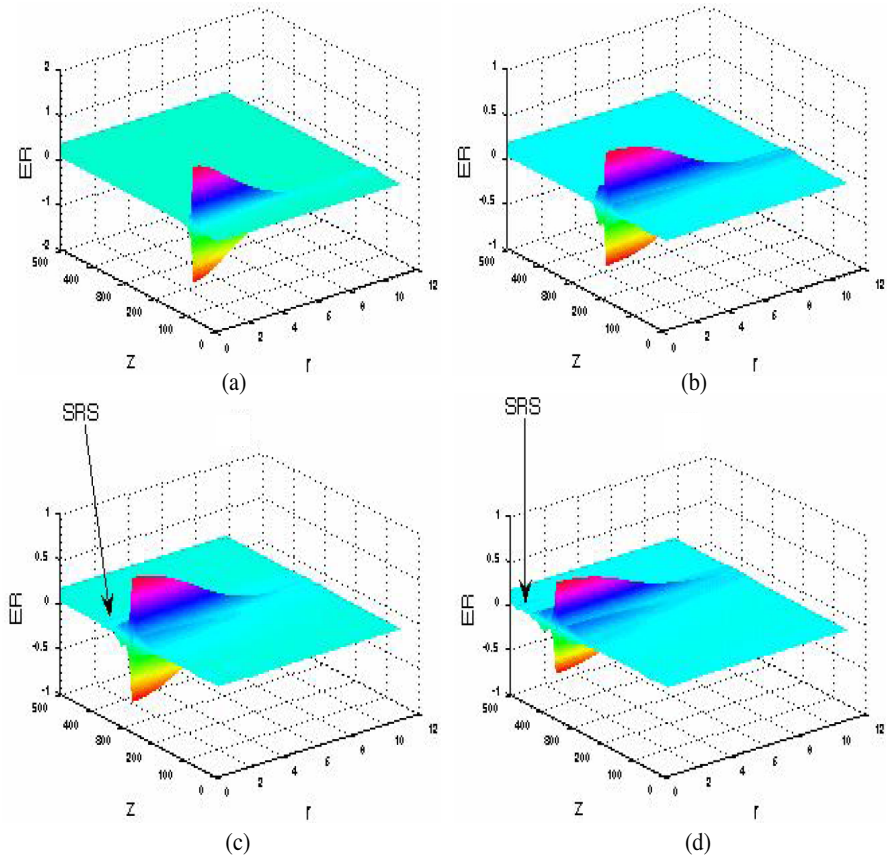

Figure 9. Spatial variation of E_r, in 30° φ-plane, at instants of: (a) 675 fs (b) 1475 fs (c) 2125 fs (d) 3250 fs.

Nonlinear susceptibility: $\chi^{(3)} = 0.07\,\mathrm{m}^2/\mathrm{V}^2$

Reciprocal of the photon frequency: $\tau_1 = 6.1\,\mathrm{fs}$

Photon lifetime: $\tau_2 = 32\,\mathrm{fs}$ sec

Relative strength of SPM to SRS is set to be: $\alpha = 0.7$

Input amplitude: $E_0 = 2.4\,\mathrm{Vm}^{-1}$ [.]

Figs. 9(a)–9(d) illustrate the behavior of E_r component at different stages of propagation. In comparison with those of Fig. 4, it is clear that both the amplitude and the width of the propagated pulse remain nearly unchanged. This means that the pulse is not dispersive as it progresses along the optical fiber. This predicted result belongs to the existence of the nonlinear effects which causes anti dispersion. The resulting anti dispersion tends to cancel out the dispersion caused by the linear effects and the combination of the two effects results in a soliton-like pulse, which means that the cancellation is not exact between the GVD and nonlinear dispersion. Additionally, it is of importance to note that there is a low intensity pulse that emerges from the leading edge of the main pulse and travels much faster than it. The

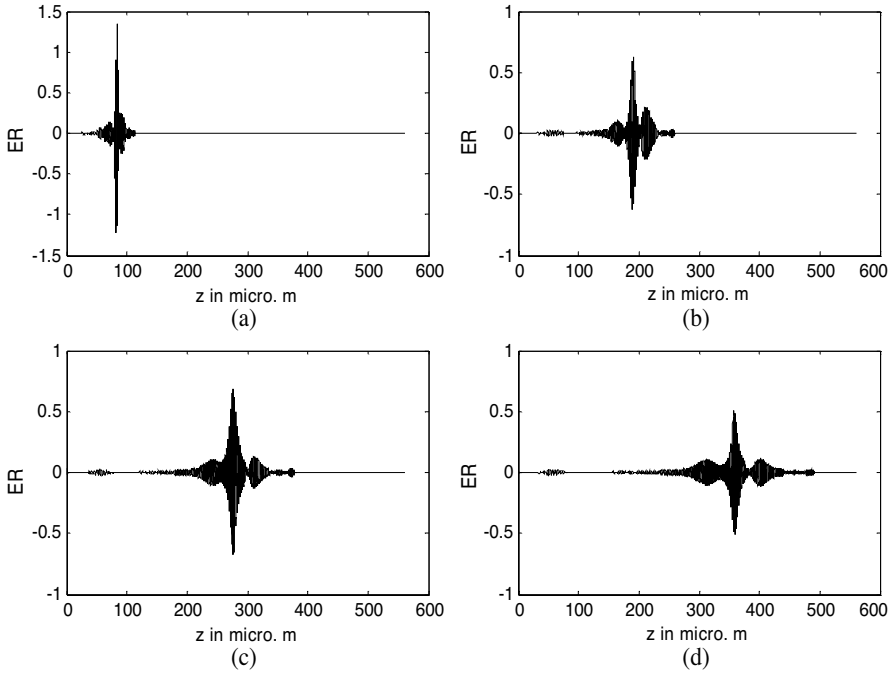

Figure 10. Axial variation of the radial component of the electric field (E_r) at instants of: (a) 675 fs (b) 1475 fs (c) 2125 fs (d) 3250 fs.

generation of this new sub-pulse is owing to the effect of Stimulated Raman Scattering SRS. Figs. 10(a)–10(d) show the same thing as Figs. 5(a)–5(d) for the present operating conditions. The comparison of this family of curves with those of linear case demonstrates the role that nonlinear effects can play in maintaining the shape of the propagated pulse through out the longitudinal direction of the optical waveguide. In addition, the effect of the appearance of the secondary low intensity pulse that propagates faster than the mother pulse is more evident. The third family of curves, Figs. 11(a)–11(d) is concerned with the radial variation of the intensity of the fundamental mode at different z values. It is apparent that the maximum value of the field, occurring at the center of the optical fiber, exceeds the unity value. The gain, that the electric field attains, is owing to the nonlinear effects and especially the SPM phenomena which have a fort influence on the behavior of the pulse than the linear effects. In addition, the envelope of the pulse has a bell shape which, approximately, rest unchanged through out the length of fiber. As an introduction to the spectrum of the field component, Figs. 12(a)–12(c) depict the time variation of the radial component of the associated field at different locations on the guide axis. The waveform of the field variation remains

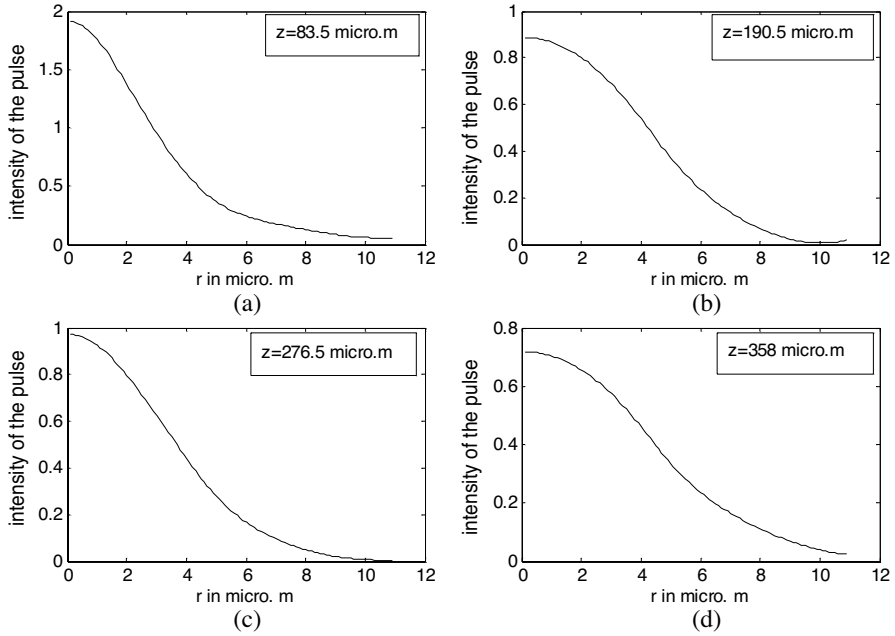

Figure 11. The peak intensity variation of the pulse at instants equal: (a) 675 fs (b) 1475 fs (c) 2125 fs (d) 3250 fs.

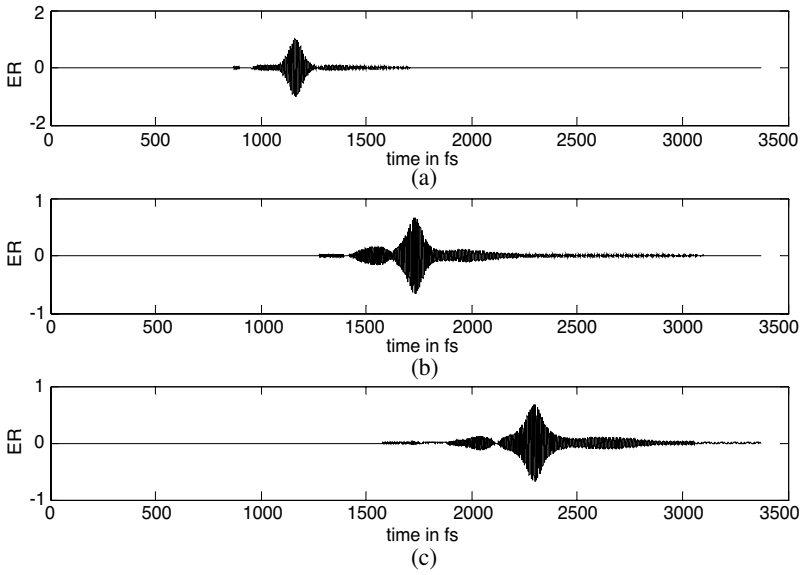

Figure 12. Temporal variation of E_r at different points on the axis and at z equals to (a) $z = 150\,\mu\text{m}$ (b) $z = 225\,\mu\text{m}$ (c) $z = 300\,\mu\text{m}$.

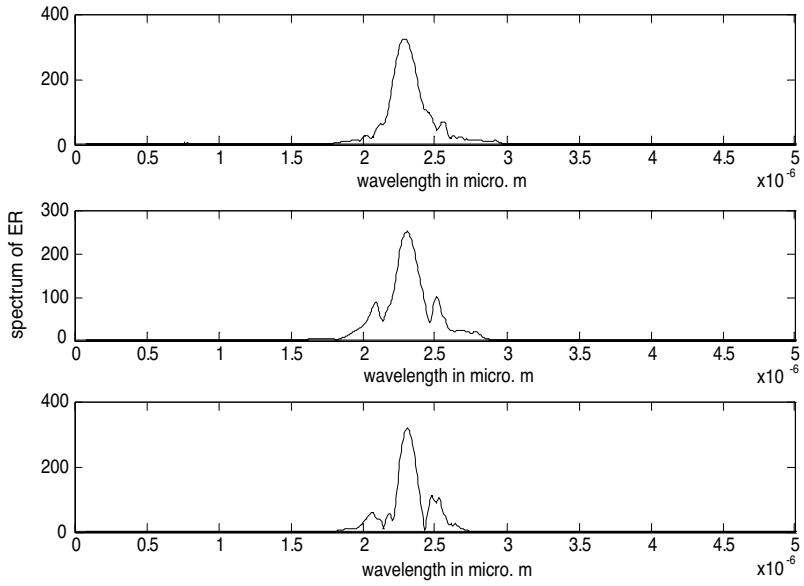

Figure 13. Spectrum of E_r at different points on the axis and at z equals: (a) $150\,\mu\text{m}$ (b) $225\,\mu\text{m}$ (c) $300\,\mu\text{m}$.

approximately of the same form without significant changes. As a final step in our evaluation procedure, Figs. 13(a)–13(c) illustrate the frequency-domain representation corresponding to Figs. 13(a)–13(c). The comparison of this family of curves with those outlined in the previous category reveals that the central frequency of the main pulse is shifted downwards due to stimulated Raman scattering (SRS).

5. CONCLUSIONS

In this paper, we have developed a computational electromagnetic algorithm that is capable of modeling the propagation of an ultra-short pulse in an optical fiber which exhibits linear and nonlinear effects. The nonlinear effects that are taken into account include the self phase modulation SPM and the Stimulated Raman Scattering SRS. Our analysis is based on FDTD-BOR technique with direct integration method to model the dispersion and nonlinear effects. The presented results show a significant importance of the nonlinearity effect in reducing the overall dispersion along the optical fiber. The proposed algorithm can be used as a design tool for different devices such as fiber Bragg grating (FBG) which has many important practical applications.

REFERENCES

1. Agrawal, G., *Nonlinear Fiber Optics*, Academic, New York, 2001.
2. Jin, G. H., J. Harari, J. P. Vilcot, and D. Decoster, "An improved time-domain beam propagation method for integrated optics components," *IEEE Photonics Technol. Lett.*, Vol. 9, No. 3, 348–350, 1997.
3. Joseph, R. M. and A. Taflove, "FDTD Maxwell's equations models for nonlinear electrodynamics and optics," *IEEE Trans. Antennas Propag.*, Vol. 45, No. 3, 364–374, Mar. 1997.
4. Sullivan, D. M., "Nonlinear FDTD formulations using Z transforms," *IEEE Trans. Microw. Theory Techn.*, Vol. 43, No. 3, 676–682, Mar. 1995.
5. Luebbers, R., F. P. Hunsberger, K. S. Kunz, R. B. Standler, and M. Schneider, "A frequency-dependent finite difference time-domain formulation for dispersive media," *IEEE Trans. Elect. Mag. Compat.*, Vol. 32, No. 3, 222–227, Aug. 1990.
6. Goorjian, P. M., A. Taflove, R. M. Joseph, and S. C. Hagness, "Computational modeling of femtosecond optical solitons from Maxwell's equations," *IEEE J. Quantum Electronics*, Vol. 28, No. 10, 2416–2422, Oct. 1992.

7. Joseph, R. M., P. M. Goorjian, and A. Taflove, "Direct time integration of Maxwell's equations in 2-D dielectric waveguides for propagation and scattering of femtosecond electromagnetic solitons," *Opt. Lett.*, Vol. 18, 491–493, Apr. 1993.
8. Zhou, D., W. P. Huang, C. L. Xu, D. G. Fang, and B. Chen, "The perfectly matched layer boundary condition for scalar finite-difference time-domain method," *IEEE Photonics Technol. Lett.*, Vol. 13, No. 5, 454–456, May 2001.
9. Sullivan, D., J. Liu, and M. Kuzyk, "Three-dimensional optical pulse simulation using the FDTD method," *IEEE Trans. Microw. Theory Techn.*, Vol. 48, No. 7, 1127–1133, July 2000.
10. El Mashade, M. B., M. Ashry, and A. Nasr, "Theoretical analysis of quantum-dot infrared photodetectors," *Semicond. Sci. Technol.*, Vol. 18, 891–900, 2003.
11. Buchanan, W. J., "Analysis of electromagnetic wave propagation using the 3D finite-difference time domain method with parallel processing," Ph.D. Thesis, Napier University, Mar. 1996.
12. Taflove, A. and S. C. Hagness, *Computational Electrodynamics: The Finite Difference Time-domain Method*, Artech House, Boston, 2000.
13. Pérez-Ocón, F., A. M. Pozo, J. R. Jiménez, and E. Hita, "Fast single-mode characterization of optical fiber by finite-difference time-domain method," *J. Light Wave Technology*, Vol. 24, No. 8, 3129–3136, Aug. 2006.
14. Crando, J., "FDTD computation of dispersive effects for a body of revolution," *IEEE Antennas and Propagation Society International Symposium*, Vol. 1, 48–51, July 8–13, 2001.
15. Chen, Y., R. Mittra, and P. Harms, "Finite-difference time-domain algorithm for solving Maxwell's equations in rotationally symmetric geometries," *IEEE Trans. Microw. Theory Techn.*, Vol. 44, No. 6, 832–839, June 1996.
16. Blow, K. and D. Wood, "Theoretical description of transient stimulated Raman scattering in optical fibers," *IEEE J. Quantum Electronics*, Vol. 25, No. 12, 2665–2673, Dec. 1989.